PAPER

CrossMark
click for updates

Sn(II,IV) steric and electronic structure effects enable self-selective doping on Fe/Si-sites of Li₂FeSiO₄ nanocrystals for high performance lithium ion batteries†

Kai Wang,‡ Gaofeng Teng,‡ Jinlong Yang,‡ Rui Tan, Yandong Duan, Jiaxin Zheng and Feng Pan*

We report Sn(II) and Sn(IV) self-selective dual-doping, respectively, on Fe and Si sites of Li₂FeSiO₄ nanocrystals due to the steric and electronic structure effects of Sn(II,IV). Combined with experimental studies and theoretical calculations, we investigate the structure–property relationship of tin doped Li₂FeSiO₄ as the cathode material for high performance Li-ion batteries, in which the dual-doping enhances the electronic conductivity and lithium-ion diffusion coefficient. The doped sample with 5% Sn(IV) source shows the best electrochemical performance due to the improved electronic conductivity and Li-ion diffusivity. Density functional theory (DFT) calculations also reveal that tin dual-doped Li₂FeSiO₄ has better electronic conductivity and lower voltage of delithiation than that of the undoped Li₂FeSiO₄, which is in accordance with our experimental results.

Introduction

The application of lithium-ion batteries has been expanded from portable electronics to stationary energy storage systems and automotive power sources.[1–3] However, the performance of lithium ion batteries is limited by the cathode material. Traditional cathode materials, such as layered Li transition metal oxides, spinel-structural manganate and olivine-structural phosphate, cannot satisfy the need of next-generation lithium-ion batteries. There is an urgent demand to search for cathode materials for rechargeable lithium-ion batteries with high energy density, high safety, and low cost.[4–6] Lithium iron silicate (Li₂FeSiO₄), with iron and silicon being among the most abundant and lowest cost elements, attracts the most interest.[7] Specially, Li₂FeSiO₄ has about two times higher theoretical capacity (166/332 mA h g⁻¹ for one/ two Li⁺ intercalation/deintercalation, respectively) than that of LiFePO₄ (170 mA h g⁻¹).[8–10] Moreover, the strong covalent nature of the Si–O bonds in Li₂FeSiO₄ should lead to safer and more stable cycling than that of the P–O bonds in LiFePO₄.[11]

However, some features, such as the slow lithium-ion diffusion coefficient ($\sim 1 \times 10^{-14}$ cm² s⁻¹ at 25 °C)[12] and low intrinsic electronic conductivity ($\sim 6 \times 10^{-14}$ S cm⁻¹ at 25 °C)[11], have limited the large scale applications of Li₂FeSiO₄ in commercial Li-ion batteries, which makes the insertion/extraction of lithium ions into/from the lattice difficult. In order to overcome these drawbacks, lot of efforts such as carbon coating,[13,14] scaling the particle to nanoscale[13] and heteroatom doping have been applied. Heteroatom doping with Al³⁺,[15] Cd²⁺,[16] Co²⁺,[17] Zn²⁺, Cu²⁺ and Ni²⁺[18] has shown an efficient way to enhance the Li-ion diffusion coefficient and electronic conductivity of Li₂FeSiO₄.

In this work, we report for the first time doped Li₂FeSiO₄ with two different valence state tin (Sn(II) and Sn(IV)) sources by a typical sol–gel method. We found that tin had significant characteristics of self-selective doping due to the Sn(II,IV) steric and electronic structure effects, Sn(II) only occupies Fe sites, and Sn(IV) occupies Si sites in Li₂FeSiO₄. By using an Sn(IV) source, Li₂FeSiO₄ nanocrystals with the Sn(II) and Sn(IV) self-selective dual-doping, respectively, on Fe and Si sites are formed. DFT calculations also proved that tin doping can lower the delithiation voltage, promoting the extraction of more Li-ions from Li₂FeSiO₄ within the stable windows of an electrolyte to enhance the cell capacity. The Sn(II,IV) self-selective dual-doping of Li₂FeSiO₄ exhibits the recorded high-capacity (311.5 mA h g⁻¹ at 0.2C), high-rate performance (156.9 mA h g⁻¹ at 10C) and long life-time (remaining 96.0% after 500 cycles) making it a promising next-generation cathode material for high-power lithium-ion batteries.

School of Advanced Materials, Peking University Shenzhen Graduate School, Shenzhen 518055, People's Republic of China. E-mail: panfeng@pkusz.edu.cn

† Electronic supplementary information (ESI) available: XRD patterns, SEM image EDS mapping, and Raman, TG and BET analyses; calculated lattice parameters using DFT; XRD with chemical extraction of lithium. See DOI: 10.1039/c5ta06713h

‡ These authors contributed equally to this work.

Experimental

1. Synthesis of pure and tin-doped Li₂FeSiO₄/C composites

The pristine Li₂FeSiO₄/C sample and tin-doped samples were synthesized by sol–gel methods as we reported earlier.[12] For the

pristine Li_2FeSiO_4/C sample, 18 mmol of $Fe(NO_3)_3 \cdot 9H_2O$ (SCRC, China) and 36 mmol of $LiAc \cdot 2H_2O$ (SCRC, China) were dissolved in 60 mL of deionized water, then 18 mmol of tetraethyl orthosilicate (TEOS) (Aladdin) dissolved in 30 mL ethanol was added with constant stirring, finally 18 mmol of citric acid dissolved in 30 mL of deionized water was added into the aforementioned solution with a dropping funnel. After stirring under 60 °C continuously for 24 hours, the solution was dried at 80 °C to form xerogel and then ground by mechanical ball milling for 10 hours. Finally the milled powder was pressed into pellets and calcinated at 650 °C for 10 h under a fixed argon flux to obtain the Li_2FeSiO_4/C sample. $SnSO_4 \cdot 2H_2O$ (1%, 3%, 5%, 7% and 10% of 18 mmol, Aladdin, Sn(II) source) and $SnCl_4 \cdot 5H_2O$ (1%, 3%, 5%, 7%, 10% and 20% of 18 mmol, Aladdin, Sn(IV) source) were added into the solution just after the addition of $Fe(NO_3)_3 \cdot 9H_2O$ (its amount decreases accordingly with the amount of tin), by which Sn(II) and Sn(IV) source-doped Li_2FeSiO_4/C samples were synthesized. Other processes were the same as the synthesis process of the Li_2FeSiO_4/C sample.

2. Material characterization

X-ray patterns were collected using a Bruker D8-Advance diffractometer (40 kV, 40 mA Cu Kα). Rietveld refinements were performed to determine the lattice parameters and atomic site occupancy for the synthesized samples using the TOPAS 4.2 package. Scanning electron microscopy (SEM) images were taken with a ZEISS SUPRA®55 field emission SEM and energy dispersive X-ray spectra (EDS) were tested using OXFORD Aztec instruments. Transmission electron microscope (TEM) images were obtained on a FEI Tecnai G2F30. Raman Spectra were collected using a Horiba iHR 320. Thermal gravimetric (TG) analysis was performed with a Mettler Toledo TGA/DSC1 analyzer at a heating rate of 10 °C min^{-1}. The specific surface areas were analyzed using Brunauer–Emmett–Teller (BET) nitrogen adsorption–desorption measurements with a Micromeritics ASAP 2020 HD88 and the X-ray photoelectron spectroscopy (XPS) data were collected using a Thermo Fisher ESCALAB 250X.

3. Theoretical calculations

All of the calculations were performed using DFT with the exchange-correlation functional treated in the spin-polarized GGA as parameterized by Perdew, Burke and Ernzerhof (PBE)[19] using a projected augmented wave (PAW) method as implemented in the Vienna Ab initio Simulation Package (VASP).[20,21] The energy cut-off for the plane wave basis set was kept fixed at a constant value of 520 eV throughout our calculations. The integration in the Brillouin zone is done on a set of k-points determined by the Monkhorst and Pack theme:[22] $3 \times 3 \times 3$ for all systems, using the energy and force convergence criteria $<10^{-5}$ eV and <0.03 eV Å^{-1}. The PBE + U approach[23] is employed to take account of the strong on-site Coulomb interaction (U) presented in the localized 3d electrons of Fe, and an effective U value of 4.3 eV was used.

4. Electrochemistry

Coin (CR2016) cells were assembled in an argon-filled glove-box with metallic lithium as the anode, Celgard 2400 polypropylene as the separator, and 1 M $LiPF_6$ in EC and DMC (1 : 1 by volume) as the electrolyte. The cathode materials were prepared by mixing the active material : Ketjen black : poly-tetrafluoro-ethylene (PTFE) in the ratio of 7 : 2 : 1. Galvanostatic charge/discharge measurement was performed in the potential range from 1.5 to 4.8 V vs. Li/Li$^+$ with a LAND CT2001A multichannel battery testing system. The specific capacity was calculated on the basis of the amount of the active material, excluding the mass of the coated carbon of the samples. Cyclic voltammetry (CV) was performed using a CHI 660e electrochemical workstation, and the electrochemical impedance spectrum (EIS) was tested with a Princeton ParStat 2273. All the above-mentioned electrochemical tests were carried out at a room temperature of 30 °C.

Results and discussion

The X-ray diffraction patterns of the synthesized samples are shown in Fig. 1 and S1.† Fig. 1 shows that the Sn(II) and Sn(IV)-doped samples are very similar to the pristine Li_2FeSiO_4/C sample, which are indexed to the monoclinic structure with a (γ$_s$) $P2_1/n$ space group.[24] Observing from Fig. S1,† for the Sn(IV)-doped samples, the doping ratio is up to 7% without any impurities, and for the Sn(II)-doped samples it is up to 5%. The (020) peak offset in both XRD patterns of Sn(II) and Sn(IV)-doped samples (Fig. S1c†) display that tin has affected the inter-lamellar spacing of the Li_2FeSiO_4 crystal. The SEM images of the three samples are shown in Fig. 2a–c and S2.† All the samples are micron-sized agglomerates (Fig. S2a†), which are composed of nano-sized particles (Fig. 2a–c). The size distributions are shown in the insets of Fig. 2a–c. The average sizes of the pristine, Sn(II) and Sn(IV)-Li_2FeSiO_4/C samples are 114, 108 and 95 nm, respectively. The energy-dispersive X-ray spectroscopy (EDS) mappings in Fig. 2d–i and S3† show that tin was uniformly distributed throughout the crystal of the Sn(IV) and Sn(II)-Li_2FeSiO_4/C samples.
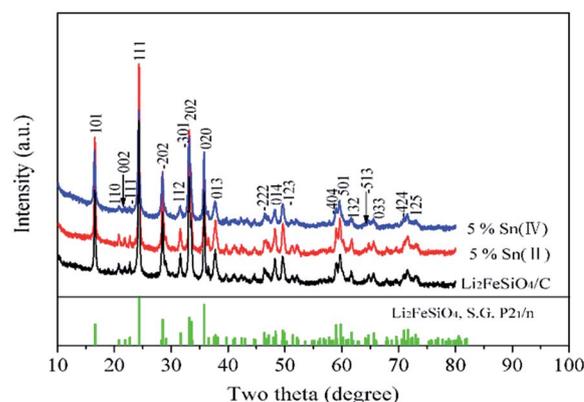
Fig. 1 XRD patterns of Li_2FeSiO_4/C, 5% Sn(II)-Li_2FeSiO_4/C and 5% Sn(IV)-Li_2FeSiO_4/C.
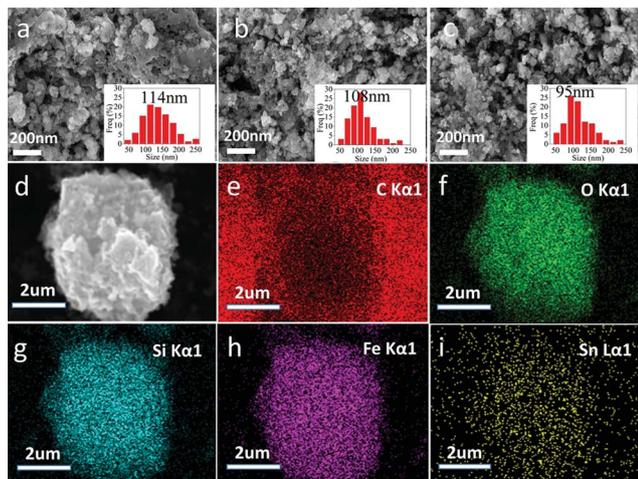
Fig. 2 SEM images and size distributions (insets) of (a) Li_2FeSiO_4/C, (b) 5% Sn(II)-Li_2FeSiO_4/C and (c) 5% Sn(IV)-Li_2FeSiO_4/C; (d–i) EDS mappings of 5% Sn(IV)-Li_2FeSiO_4/C.

Fig. 3 TEM and HRTEM images of (a and d) Li_2FeSiO_4/C, (b and e) 5% Sn(II)-Li_2FeSiO_4/C and (c and f) 5% Sn(IV)-Li_2FeSiO_4/C. The measured crystal sizes are shown in TEM images.

The transmission electron microscopy (TEM) images of the pristine, Sn(II) and Sn(IV)-Li_2FeSiO_4/C samples are shown in Fig. 3. Observing from Fig. 3a–c, the crystal particles are coated around by amorphous carbon, the crystal sizes are well in agreement with those determined by the Scherrer formula from XRD data, the sizes of Sn(II)-Li_2FeSiO_4 (43–46 nm) and Sn(IV)-Li_2FeSiO_4 (36–41 nm) crystals are smaller than that of the pristine Li_2FeSiO_4 (52–79 nm) crystal. The small crystal sizes of Sn-doped Li_2FeSiO_4 crystals can enhance electrochemical performance. The high resolution-transmission electron microscopy (HRTEM) images (Fig. 3d–f) show that all the samples display clear lattice fringes corresponding to the different planes of monoclinic structural Li_2FeSiO_4. In Fig. 3d and f, the crystal planes with a *d*-spacing of 0.267 nm correspond to the (202) planes, and in Fig. 3e, those with 0.251 nm correspond to the (020) planes, indicating that all samples have good crystallinity. In addition, it can be clearly seen that the amorphous carbon is uniformly coated on the crystal surface and possesses a thickness of 2–5 nm. Thermal gravimetric analysis (Fig. S4†) shows that the carbon contents of all the three samples are very similar, about 13.5%. The carbon structure was further revealed using Raman spectra. As shown in Fig. S5,† the bands at 1347 and 1590 cm^{-1} can be assigned to the D-band and G-band of carbon materials, and the intensity ratio of D and G bands is usually used to evaluate the electronic conductivity of the residual carbon.[25] The peak intensity ratios of the D to G bands (I_D/I_G) are 1.21, 1.22 and 1.18, respectively. These similar I_D/I_G values indicate that tin doping does not obviously affect the electronic conductivity of the carbon. These coated carbons could provide an excellent conductive network to enhance the cell performance. Nitrogen adsorption and desorption isotherms are shown in Fig. S6.† It can be seen that the determined Brunauer–Emmett–Teller (BET) surface areas of Li_2FeSiO_4/C, 5% Sn(II)-Li_2FeSiO_4/C and 5% Sn(IV)-Li_2FeSiO_4/C are 42.4, 44.5 and 59.1 m^2 g^{-1}, respectively, indicating that these nanomaterials as cathodes possessed excellent contact
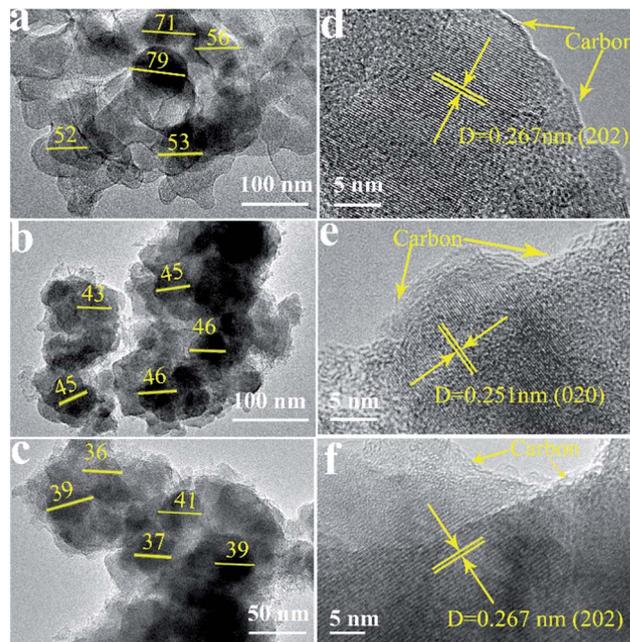
with the conductive agent and electrolyte to obtain high rate performance for lithium ion batteries.[26,27]

X-ray photoelectron spectroscopy (XPS) spectra are used to investigate the oxidation state of component elements in samples, and it can also be used to detect the distribution of component elements at the surface or/and inside of the samples by argon ion sputtering.[16] The XPS full-spectra in the interior of Li_2FeSiO_4/C, 5% Sn(II)-Li_2FeSiO_4/C and 5% Sn(IV)-Li_2FeSiO_4/C are shown in Fig. S7.† In this work, all the binding energies are referenced to the C 1s peak at 284.6 eV. The XPS spectrum of Li_2FeSiO_4/C exhibits six characteristic peaks corresponding to Li 1s, Fe 2p, Si 2s, Si 2p, C 1s and O 1s. Besides the mentioned peaks, Sn 3d peaks are shown in the XPS spectra of both 5% Sn(II)-Li_2FeSiO_4/C and 5% Sn(IV)-Li_2FeSiO_4/C. The Fe 2p spectra (inset of Fig. S7†) showed that tin doping did not affect the valence state of iron in Li_2FeSiO_4, and the oxidation state of Fe in all of the three samples is Fe(II). In addition, as shown in Fig. S8,† with the doping of tin, the binding energy of Li 1s is similar to 55.92 eV (Li_2FeSiO_4/C) and 55.90 eV (5% Sn(II)-Li_2-$FeSiO_4$/C), but obviously decreased to 55.69 eV (5% Sn(IV)-Li_2-$FeSiO_4$/C),[28] which could be more favorable for Li extraction from the crystal, resulting in the increased lithium-ion diffusion coefficient. The binding energies of Sn 3d 5/2 in the 5% Sn(II)-Li_2FeSiO_4/C and 5% Sn(IV)-Li_2FeSiO_4/C samples are shown in Fig. 4. The Sn 3d 5/2 line could be further fitted by two sub-peaks with binding energies of 486.5 eV and 487.1 eV, which correspond to the Sn^{2+} (Sn(II)) and Sn^{4+} (Sn(IV)), respectively.[29–32] For the 5% Sn(II)-Li_2FeSiO_4/C sample, the interior of the sample shows 100% of Sn(II), although two different valence states (Sn(II) and Sn(IV)) of tin are observed at the surface due to the oxidation of the sample in air (Fig. 4). For the 5% Sn(IV)-Li_2FeSiO_4/C sample,

there exists two valence states, 35.2% of Sn(II) and 64.8% of Sn(IV) at the surface (Fig. 4c), and 41.6% of Sn(II) and 58.4% of Sn(IV) in the interior (Fig. 4d). With the Sn(IV) source to dope samples, the presence of Sn(II) can be attributed to the reduction of citric acid in solution and carbothermic reduction at high temperature in our synthetic process. Interestingly, with the increase of the doping amount of the Sn(IV) source, the amount of Sn(II) decreases and that of Sn(IV) increases (shown in Fig. 4e–h and Table S1†) in the interior of the Sn(IV)-Li_2FeSiO_4/C samples, which could be attributed to the Sn(II,IV) steric effect.

Full Rietveld refinement was carried out on the Li_2FeSiO_4, 5% Sn(II)-Li_2FeSiO_4 and 5% Sn(IV)-Li_2FeSiO_4. The XRD patterns with a slow scan speed (2 s per step of 0.02° increment) confirmed the phase purity with no impurity peaks being detected and were used for Rietveld refinement (shown in Fig. 5). The refined atomic coordination and lattice parameters are listed in Table S2† and Table 1, respectively. The best refinement model was chosen from the $P2_1/n$ space group.[24] For Li_2FeSiO_4 (Table S2.1†), the reliable factors, R_p is 0.71%, and R_{wp} is 0.92%, which are less than 1%, indicating the Rietveld refinement results are reliable in the following analysis of the crystal structure. For tin-doped Li_2FeSiO_4 samples, when all the atomic positions of Li, Fe, and Si are opened for Sn(II) and/or Sn(IV) atoms during the Rietveld refinement, Sn(II) atoms prefer to occupy the Fe site, but Sn(IV) atoms prefer to occupy the Si site, indicating Sn(II,IV) self-selective doping to Li_2FeSiO_4 nanocrystals. The mechanism could be that Sn(II) and Sn(IV) have closely steric and electronic structures compared to those of Fe(II) and Si(IV), respectively, due to their cationic radius and valence states. The tetrahedral coordination radius of Sn(II) ([Kr] $4d^{10}5p^2$, 1.00 Å) is larger than that of Fe(II) ([Ar]$3d^6$, 0.59 Å) about 0.41 Å but their valences are the same with 2+ so that the valence and composition equilibrium can be maintained. On the other hand, the tetrahedral cationic radius of the Sn(IV) ([Kr] $4d^{10}$, 0.57 Å) is larger than that of Si(IV) ([Ne], 0.26 Å) about 0.31 Å, but both of them possess a similar electronic structure with full

electrons in the outermost orbit (the detailed effective radius in tetrahedra are shown in Table S3†). Based on Hund's rule and the minimal energy principle, the Sn(IV) doped at the Si site retains its valences even when Li-ions are all extracted (which are proved by subsequent DFT calculations afterwards), still to maintain the stable structure. The detailed structural parameters obtained from Rietveld refinement of 5% Sn(II)-Li_2FeSiO_4 and 5% Sn(IV)-Li_2FeSiO_4 are listed in Tables S2.2 and S2.3,† respectively. For the 5% Sn(II)-Li_2FeSiO_4, R_p and R_{wp} are 0.83% and 1.08%, respectively, and for the 5% Sn(IV)-Li_2FeSiO_4, R_p and R_{wp} are 0.73% and 0.94%, respectively. Very low R_p and R_{wp} (reliability factor of structure factors) strongly support the doped structural model. As shown in Table 1, the unit cell volume increases after Sn doping. The cell volume change with the Sn doping can be explained by the ionic size of Sn(II) to be much larger than that of Fe(II), so that the 5% Sn(II)-Li_2FeSiO_4

Fig. 5 Rietveld refinement of the XRD pattern of the $P2_1/n$ space group Li_2FeSiO_4. Bottom: material Li_2FeSiO_4, middle: material 5% Sn(II)-Li_2FeSiO_4, and top: 5% Sn(IV)-Li_2FeSiO_4. The blue crosses, red line, and gray line represent the observed, calculated, and difference patterns, respectively. The positions of the Bragg reflections are shown as vertical blue bars.

Fig. 4 (Left) Fitted Sn 3d 5/2 spectra of (a) surface of 5% Sn(II)-Li_2FeSiO_4/C, (b) interior of 5% Sn(II)-Li_2FeSiO_4/C, (c) surface of 5% Sn(IV)-Li_2FeSiO_4/C, and (d) interior of 5% Sn(IV)-Li_2FeSiO_4/C; (Right) fitted Sn 3d 5/2 spectra of different ratios of Sn(IV) doped Li_2FeSiO_4/C samples: (e) 1%, (f) 3%, (g) 5%, and (h) 7%.

Table 1 Refined lattice parameters of Li_2FeSiO_4, 5% Sn(II)- and Sn(IV)-Li_2FeSiO_4

Sample	a (Å)	b (Å)	c (Å)	β (deg)	V (Å^3)
Li_2FeSiO_4	8.2417	5.0140	8.2248	98.9467	335.754
5% Sn(II)	8.2423	5.0131	8.2364	98.8885	336.237
5% Sn(IV)	8.2278	5.0173	8.2432	99.0112	336.099

possesses the largest cell volume due to the high amount of doped Sn(II).

Based on the previous studies,[33] Li_2FeSiO_4 will undergo phase transformation with a significant structure change driven by an electrochemical process. Once half the amount of Li ions is extracted during discharge at the first few times, all the Fe ions (site 2a) will be interchanged to Li sites (site 4b), the phase transformation of the material occurs from an initial $P2_1/n$ structure (γ_s) to an inverse-$Pmn2_1$ structure (inverse-β_{II}), which will be stabilized after the initial few charge–discharge cycles. The same structure change also appeared in the Sn-doped samples, which could be observed and proved from the initial two cyclic voltammetry (CV) curves and charge–discharge profiles (Fig. 8a and b and S10†). The stable structure with the inverse-$Pmn2_1$ space group was adopted for DFT calculations. In our calculation, the cycled stable structure (labeled as inverse βII) is employed,[34] which is also carried out to understand the effect of tin doping in Li_2FeSiO_4 for the first time. A $2 \times 2 \times 2$ Li_2FeSiO_4 supercell model containing 16 Fe atoms and 16 Si atoms was constructed. The 6.25% Sn doping was achieved by replacing one of the 16 Fe or Si atoms in the supercell by Sn (all the Fe sites or Si sites are equivalent).

Calculated crystal structures of Li_2FeSiO_4, $Li_2Fe_{0.94}Sn_{0.06}SiO_4$ and $Li_2FeSi_{0.94}Sn_{0.06}O_4$ are shown in Fig. 6. Our calculated lattice parameters of Li_2FeSiO_4 are consistent with the theoretical and experimental results reported by G. Bruce.[34] The structure parameters of Li_xFeSiO_4, $Li_xFe_{0.94}Sn_{0.06}SiO_4$ and Li_x-$FeSi_{0.94}Sn_{0.06}O_4$ ($x = 2, 1, 0.5$ and 0) are listed in Table S4.† Compared to pristine Li_2FeSiO_4, the cell volume of $Li_2Fe_{0.94}$-$Sn_{0.06}SiO_4$ is 0.8% larger and $Li_2FeSi_{0.94}Sn_{0.06}O_4$ is 0.9% larger. Extraction of the first lithium from Li_2FeSiO_4 is accompanied by a small volume expansion of 2.98% for Li_2FeSiO_4, 2.77% for $Li_2Fe_{0.94}Sn_{0.06}SiO_4$ and 3.19% for $Li_2FeSi_{0.94}Sn_{0.06}O_4$. If one and a half lithium had been extracted, the expansion rate is 8.17% for Li_2FeSiO_4, 7.52% for $Li_2Fe_{0.94}Sn_{0.06}SiO_4$ and 8.40% for Li_2-$FeSi_{0.94}Sn_{0.06}O_4$. However, the fully delithiated structures of the three samples experienced great distortion due to the large electrostatic repulsion between highly oxidized cations. The volume expansion rate is above 20% for the three samples.

Density of states (DOS) are shown in Fig. 6. It can be seen that the band gaps of Li_2FeSiO_4, $Li_2Fe_{0.94}Sn_{0.06}SiO_4$, and Li_2-$FeSi_{0.94}Sn_{0.06}O_4$ are 1.95, 1.88 and 1.34 eV, respectively, indicating that tin-doped Li_2FeSiO_4 shows better electronic conductivity than that of the undoped Li_2FeSiO_4 with narrowed band gaps, especially when tin is doped in Si sites. The narrowed band gaps in $Li_2Fe_{0.94}Sn_{0.06}SiO_4$ and $Li_2FeSi_{0.94}Sn_{0.06}O_4$ can be attributed to the more extensional electron orbitals and weaker hybridization between Sn orbitals and O orbitals. The average open circuit voltage can be determined by:

$$V = -\{G[Li_2FeSiO_4] - G[Li_xFeSiO_4] - (2 - x)G[Li]\}/(2 - x)E \quad (1)$$

Typically, the free energies (G) may be replaced by the ground state energies (E) with little error. Metallic lithium was used to calculate the chemical potential of a single lithium atom $\mu(Li)$.[34,35] The average voltage for $x = 1, 0.5$ and 0 was calculated. As shown in Table 2, the average voltages are lowered when tin is doped in Li_2FeSiO_4 at Fe sites and nearly kept unchanged for the tin doped at Si sites. The lowered voltage after Sn doped at the Fe sites can be attributed to the fact that the unbonded two extra electrons of Sn will be transferred little to Fe and Li atoms, thus leading to weakened Li–O bonds and lowered voltage. This would also promote the Fe^{2+} oxidation during the delithiation.

In $Li_2Fe_{0.94}Sn_{0.06}SiO_4$, the projected density of states (PDOS) shows that the O-2p and Sn-5s hybridized peak crosses the Fermi level with the first Li extraction (Fig. 7a). At the same time, the Sn–O bond length changes from 2.28 Å to 1.98 Å (Fig. S9†). This indicates that Sn changes its valence with the Sn^{2+}/Sn^{4+} redox couple when the first Li is extracted. Then Fe-3d orbits are changed from a high spin (Fe^{2+}, $3d^6$) state to a high spin (Fe^{3+}, $3d^5$) state with the Li-ion extraction (Fig. 7b). Thus, when the first Li in $Li_2Fe_{0.94}Sn_{0.06}SiO_4$ is extracted, the Sn^{2+}/Sn^{4+} oxidation occurs prior to completion, then Fe^{2+}/Fe^{3+} oxidation starts.
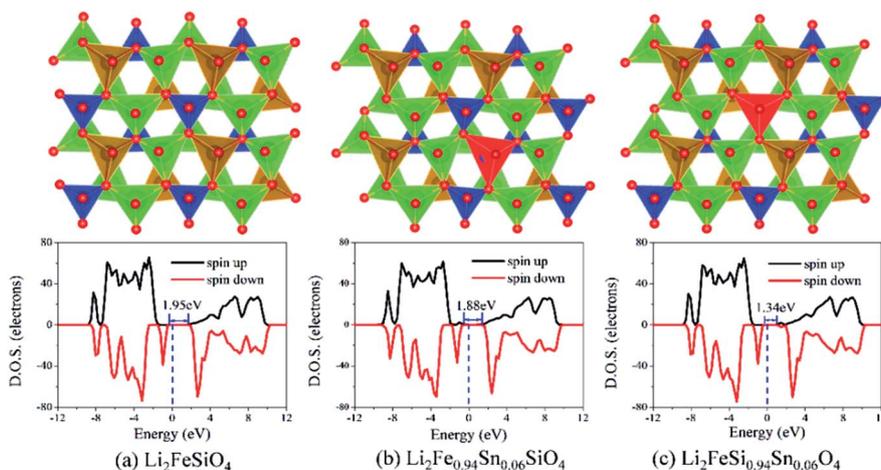
Fig. 6 Crystal structures (top panel) and spin-polarized DOS (bottom panel) for (a) Li_2FeSiO_4, (b) $Li_2Fe_{0.94}Sn_{0.06}SiO_4$ and (c) $Li_2FeSi_{0.94}Sn_{0.06}O_4$. All tetrahedra point in the same direction along the c-axis and are linked only by corner-sharing (blue: SiO_4 tetrahedra, brown: FeO_4 tetrahedra, red: SnO_4 tetrahedra, and green: LiO_4 tetrahedra). The fermi level is set at zero.

Table 2 Average voltages for the samples from the DFT calculation

Removal Li	Li_2FeSiO_4	$Li_2Fe_{0.94}Sn_{0.06}SiO_4$	$Li_2FeSi_{0.94}Sn_{0.06}O_4$
50%	2.70 V	2.64 V	2.70 V
75%	3.44 V	3.31 V	3.43 V
100%	3.76 V	3.65 V	3.75 V

The Sn^{2+}/Sn^{4+} and Fe^{2+}/Fe^{3+} oxidation can also be validated from Bader charge analysis (Table 3), which shows that the change of charge per Sn atom is 1.07 while that on the Fe atom (average) is 0.51 during the process of delithiation. Additionally, the change of the valence state from Sn^{2+} to Sn^{4+} due to the steric effect would induce heavier lattice distortion and not beneficial for the structure stability of Li_2FeSiO_4 during the delithiation. With the second Li extraction (Fig. 7c, bottom), we can see that O-2p states cross the Fermi level, it indicates that O provides electrons mainly and Fe^{3+}/Fe^{4+} plays an inactive role in the process. In $Li_2FeSi_{0.94}Sn_{0.06}O_4$, PDOS shows that the O-2p and Sn-5s hybridization peak is over the Fermi level at the beginning of the process of extracting the first lithium (Fig. 7c). Further, the change of the Sn–O bond length is less than 0.01 Å and it is even smaller than the change of the Si–O bond length during the process of Li extraction, and there are no states of Si that cross the Fermi level (Fig. 7d). The evidence suggests that Sn does not change its valence with Li extraction to retain it as Sn^{4+} in $Li_2FeSi_{0.94}Sn_{0.06}O_4$.

The initial four cyclic voltammogram (CV) curves of the Li_2FeSiO_4/C, 5% Sn(IV)-Li_2FeSiO_4/C and 5% Sn(II)-Li_2FeSiO_4/C at a scan rate of 0.2 mV s^{-1} are shown in Fig. 8a and b and S10,† respectively. The anodic peaks at about ~3.6 V reflect the oxidation of Fe^{2+} to Fe^{3+} and peaks at about 4.7 V reflect the extraction of the second lithium from the crystals. However, the peak at 3.59 V shifts to a lower potential of 3.27 V in the fourth anodic process for Li_2FeSiO_4, and for the Sn(II)-Li_2FeSiO_4 and Sn(IV)-Li_2FeSiO_4, the peak at 3.44/3.45 V shifts to a lower potential of 3.07/3.08 V, demonstrating that the Li_2FeSiO_4 as well as tin-doped Li_2FeSiO_4 exhibit structural rearrangement[33] from a monoclinic Li_2FeSiO_4 to a thermodynamically stable orthorhombic Li_2FeSiO_4. Fig. 8c presents the stable CV curves of

Table 3 Bader charge on Sn, Fe, O and Si (average) atoms on delithiation of two systems

Bader charge	$x = 2$	$x = 1$	$x = 0$
$Li_xFe_{0.94}Sn_{0.06}SiO_4$			
Sn	12.65	11.67	11.58
Fe	12.66	12.21	12.15
O	7.55	7.44	7.25
Si	0.92	0.91	0.87
$Li_xFeSi_{0.94}Sn_{0.06}O_4$			
Sn	11.84	11.77	11.71
Fe	12.66	12.22	12.16
O	7.53	7.43	7.23
Si	0.93	0.91	0.87

the three samples at a scan rate of 0.3 mV s^{-1} after four cycles at 0.2 mV s^{-1}. Observing that the 5% Sn(II)-Li_2FeSiO_4/C and 5% Sn(IV)-Li_2FeSiO_4/C have lower anodic peaks at about 3.15 V and 3.18 V, respectively, than that of Li_2FeSiO_4/C (3.29 V). Though the experimental values of the cell voltages are around 0.5 V greater than the calculated results, the tendency of Sn^{2+}/Sn^{4+} prior to oxidation around 3.08 V (Fig. S10† and 8b) is in accordance with the calculated voltages during the process of delithiation (Table 2).

The charge–discharge profiles of Li_2FeSiO_4/C, 5% Sn(II)-Li_2FeSiO_4/C and 5% Sn(IV)-Li_2FeSiO_4/C at a low rate of 0.2C (1C = 166 mA g^{-1}) are shown in Fig. S11a, S11b† and 8d, respectively. The stable discharge specific capacity at the 5th cycle for 5% Sn(IV)-Li_2FeSiO_4/C is 311.5 mA h g^{-1}, corresponding to a release of 1.88 Li$^+$ per molecule, which is higher than that of Li_2FeSiO_4/C (266.8 mA h g^{-1}) and 5% Sn(II)-Li_2FeSiO_4/C (302.7 mA h g^{-1}) as well as most of the reported Li_2FeSiO_4 materials at room temperature. The rate capability and stability of long term charge–discharge cycles of these samples are depicted in Fig. 9, and Figs. S12 and 13† showed that 5% Sn(IV)-Li_2FeSiO_4/C had better performance than others. The average discharge specific capacities of 5% Sn(IV)-Li_2FeSiO_4/C at various C-rates of 1, 2, 5, and 10C were 232.3, 220.9, 189.4 and 161.9 mA h g^{-1}, respectively, and easily recovered to 238.9 mA h g^{-1} at 1C.
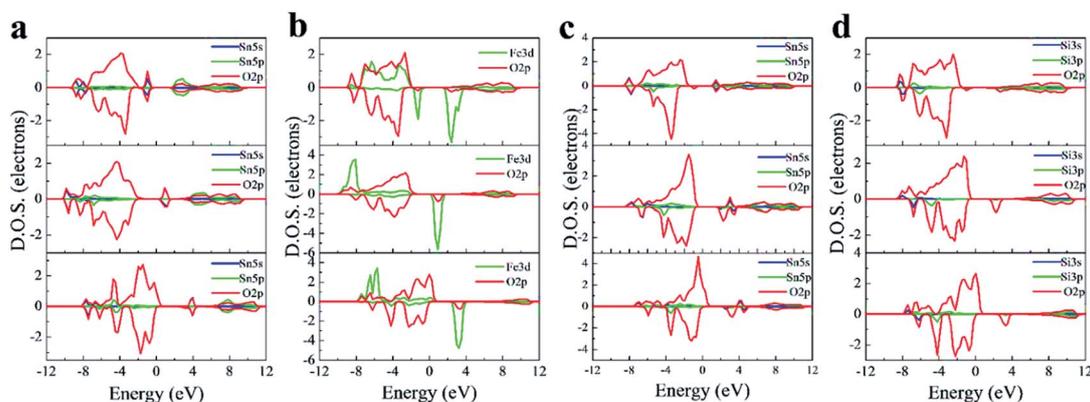
Fig. 7 Projected density of states (PDOS) of (1) (a) SnO_4 and (b) FeO_4 for $Li_xFe_{0.94}Sn_{0.06}SiO_4$; (2) PDOS of (c) SnO_4 and (d) SiO_4 for Li_x-$FeSi_{0.94}Sn_{0.06}O_4$ (from the top to the bottom, $x = 2$, 1, and 0).
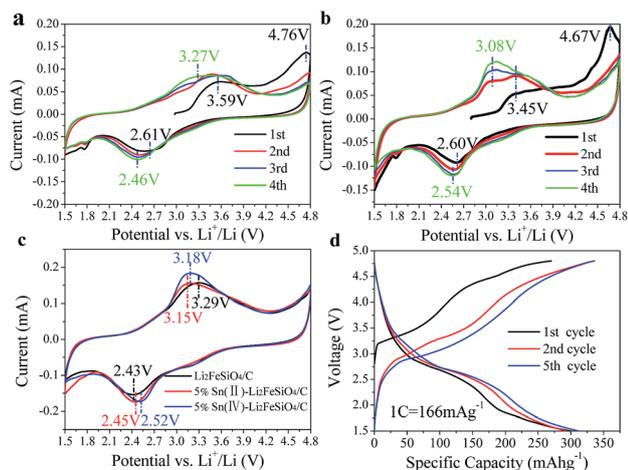
Fig. 8 Cyclic voltammograms of (a) Li_2FeSiO_4/C and (b) 5% Sn(IV)-Li_2FeSiO_4/C at 0.2 mV s^{-1}; (c) cyclic voltammograms at 0.3 mV s^{-1}; (d) charge–discharge profiles of 5% Sn(IV)-Li_2FeSiO_4/C at a low rate of 0.2C.

The electrochemical impedance spectra (EIS) were used to provide further insights into excellent high-rate capacity. The Nyquist plots for all the three samples are shown in Fig. 10a. The small intercept in the high frequency region corresponds to the resistance of the electrolyte (R_e), the depressed semicircle in the medium frequency region corresponds to the charge

transfer resistance between the electrode/electrolyte interface (R_{ct}) and the double-layer capacitance between the electrolyte and the cathode (C_{dl}), and the straight sloping line in the low frequency region is associated with lithium ion diffusion in the cathode active particles.[16] The lithium-ion diffusion coefficient can be calculated from the low frequency line according to the following equation:[36]

$$D_{Li} = R^2T^2/2A^2n^4F^4C^2\sigma^2 \qquad (2)$$

where R is the gas constant, T is the absolute temperature, A is the surface area of the cathode, n is the number of electrons per molecule during oxidization, F is the Faraday constant, C is the concentration of lithium ions, and σ is the Warburg factor to be determined from the slope of the following equation:

$$Z' = R_e + R_{ct} + \sigma\omega^{-1/2} \qquad (3)$$

The linear relationship between Z' and $\omega^{-1/2}$ in the low-frequency region is shown in Fig. 10b, and all the parameters are listed in Table 4. It can be seen that the 5% Sn(IV)-Li_2FeSiO_4/C sample has the lowest charge transfer resistance (R_{ct}) and the highest lithium diffusion coefficient (D_{Li}), which explained the excellent electrochemical performance of the 5% Sn(IV)-Li_2FeSiO_4/C. The lower R_{ct} is consistent with the results of the DFT calculation that when some Si and Fe atoms are substituted by Sn atoms, the
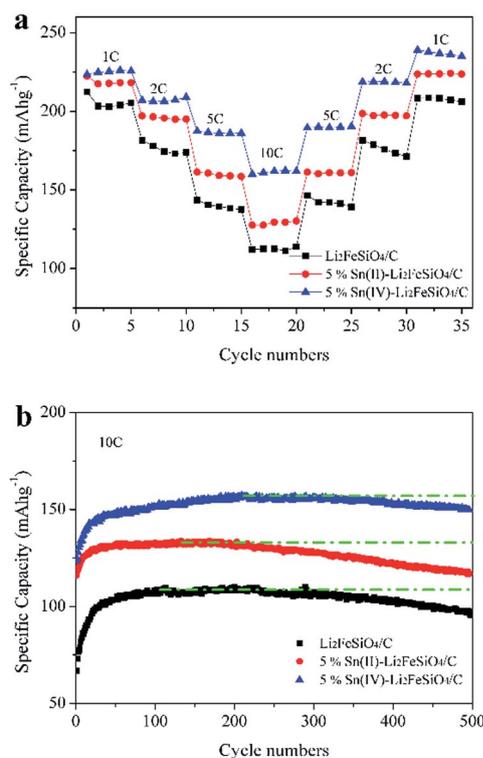
Fig. 9 (a) Cyclic performance of Li_2FeSiO_4/C, 5% Sn(II)-Li_2FeSiO_4/C and 5% Sn(IV)-Li_2FeSiO_4/C at different rates (1C → 2C → 5C → 10C → 5C → 2C → 1C); (b) long-term high rate cycling life at 10C for 500 cycles.
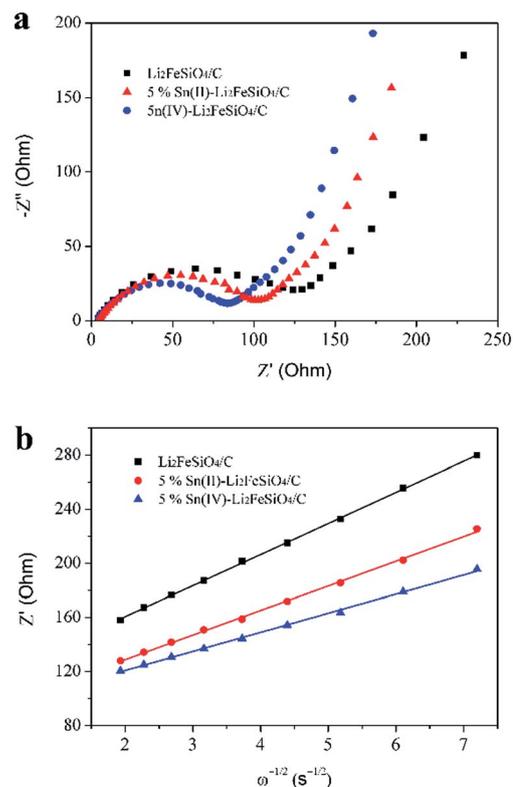
Fig. 10 (a) EIS spectra and (b) the relationship between the Z' and $\omega^{-1/2}$ in the low frequency region of Li_2FeSiO_4/C, 5% Sn(II)-Li_2FeSiO_4/C and 5% Sn(IV)-Li_2FeSiO_4/C.

Table 4 EIS parameters of Li_2FeSiO_4/C, 5% Sn(II)-Li_2FeSiO_4/C and 5% Sn(IV)-Li_2FeSiO_4/C

	Li_2FeSiO_4/C	5% Sn(II)	5% Sn(IV)
R_{ct} (Ω)	129.4	102.6	83.6
D_{Li} (cm² s⁻¹)	2.9×10^{-13}	4.7×10^{-13}	7.7×10^{-13}

sample has an obvious drop in the band gap, indicating better electronic conductivity, and the higher D_{Li}, in which the D_{Li} with 5% Sn(IV) doped is about 2.6 times higher that of undoped Li_2FeSiO_4, can be attributed to the decrease of binding energy for Li migration with the Sn doping.

The long-term high rate cyclic stability at 10C is shown in Fig. 9b. After 500 cycles, the discharge capacity of the 5% Sn(IV)-Li_2FeSiO_4/C is 150.6 mA h g⁻¹, corresponding to the capacity retention ratio of 96.0%, which is higher than that of the Li_2FeSiO_4/C (88.9%) and 5% Sn(II)-Li_2FeSiO_4/C (87.6%), meaning that the Sn(IV) self-selective dual-doping sample have better electrochemical stability than that of the Sn(II) doped and undoped Li_2FeSiO_4. To further study the structure stability vs. Li-ion extraction, samples with chemical extraction of lithium were used. The XRD patterns of the chemical extraction of lithium from all the three samples are shown in Fig. S14,† in which 5% Sn(IV)-Li_2FeSiO_4/C structures with different Li-ion extraction are the most stable with the XRD patterns. It can be seen that, after 75% and 100% of chemical extraction of lithium, some of the peaks disappeared for Li_2FeSiO_4/C. Specially, almost no peaks were observed from the 5% Sn(II)-Li_2FeSiO_4/C sample after 100% chemical extraction of lithium, indicating the crystal change to amorphous materials, which could explain the faster fading of capacity for the 5% Sn(II)-Li_2FeSiO_4/C sample. However, for the 5% Sn(IV)-Li_2FeSiO_4/C sample, the main peaks of XRD still remained after the complete extraction of lithium, indicating that the 5% Sn(IV)-Li_2FeSiO_4/C sample has a more stable structure than those of the Li_2FeSiO_4/C and 5% Sn(II)-Li_2FeSiO_4/C samples, which can support the excellent high-rate and long-life performance. In addition, the XPS of both the chemical delithiation and electrochemical delithiation further proved that the valence of Sn changed from Sn(II) to Sn(IV) previously, which agrees with our DFT calculation results that Sn(II) to replace Fe sites could change the valence state prior to the electrochemical extraction of the lithium process (Fig. S15, S16 and Table S5†).

Conclusions

Two different valence state tin (Sn(II) and Sn(IV)) had been doped into Li_2FeSiO_4 successfully by a typical sol–gel method. We found that tin had the significant characteristic of self-selective doping due to the Sn(II,IV) steric and electronic structure effects, meaning that Sn(II) only occupies Fe sites of Li_2FeSiO_4 with Sn(II) as the doping source, while both Sn(II) and Sn(IV) occupy Fe and Si sites of Li_2FeSiO_4, respectively, with Sn(IV) as the doping source. Tin-doped Li_2FeSiO_4 samples showed better electronic conductivity than that of the undoped Li_2FeSiO_4

especially when tin is doped in Si sites. Furthermore, the average voltages are lowered when tin is doped in Li_2FeSiO_4 in Fe sites, which would promote the Fe oxidation during delithiation. We also found that Sn(II) changed its valence state prior to the delithiation, which would induce heavier lattice distortion and not beneficial to the structure stability of Li_2FeSiO_4. While the valence state of Sn(IV) at Si-sites did not change with Li extraction, indicating that the doping of Sn(IV) in Si sites is more stable than the doping of Sn(II) in Fe sites for structure stability. Furthermore, 5% Sn(IV)-doped Li_2FeSiO_4 in dual Fe and Si sites shows best electrochemical performances, such as capacity, lithium-ion diffusion coefficient, charge–discharge rate and long term stability. This study indicates that tin doping is an efficient way to improve the electronic conductivity and Li-ion diffusivity of Li_2FeSiO_4 to make it a potential high capacity cathode material for next-generation Li-ion batteries.

Notes and references

1 J.-M. Tarascon and M. Armand, *Nature*, 2001, **414**, 359–367.
2 M. Armand and J.-M. Tarascon, *Nature*, 2008, **451**, 652–657.
3 C. Masquelier and L. Croguennec, *Chem. Rev.*, 2013, **113**, 6552–6591.
4 B. Dunn, H. Kamath and J.-M. Tarascon, *Science*, 2011, **334**, 928–935.
5 F. Cheng, J. Liang, Z. Tao and J. Chen, *Adv. Mater.*, 2011, **23**, 1695–1715.
6 Z. Gong and Y. Yang, *Energy Environ. Sci.*, 2011, **4**, 3223–3242.
7 A. Nyten, A. Abouimrane, M. Armand, T. Gustafsson and J. O. Thomas, *Electrochem. Commun.*, 2005, **7**, 156–160.
8 D. Rangappa, K. D. Murukanahally, T. Tomai, A. Unemoto and I. Honma, *Nano Lett.*, 2012, **12**, 1146–1151.
9 T. Muraliganth, K. Stroukoff and A. Manthiram, *Chem. Mater.*, 2010, **22**, 5754–5761.
10 J. Yang, X. Kang, L. Hu, X. Gong and S. Mu, *J. Mater. Chem. A*, 2014, **2**, 6870–6878.
11 R. Dominko, *J. Power Sources*, 2008, **184**, 462–468.
12 R. Tan, J. Yang, J. Zheng, K. Wang, L. Lin, S. Ji, J. Liu and F. Pan, *Nano Energy*, 2015, **16**, 112–121.
13 D. P. Lv, W. Wen, X. K. Huang, J. Y. Bai, J. X. Mi, S. Q. Wu and Y. Yang, *J. Mater. Chem.*, 2011, **21**, 9506–9512.
14 Z. M. Zheng, Y. Wang, A. Zhang, T. R. Zhang, F. Y. Cheng, Z. L. Tao and J. Chen, *J. Power Sources*, 2012, **198**, 229–235.
15 H. Y. Gao, Z. Hu, J. G. Yang and J. Chen, *Energy Technol.*, 2014, **2**, 355–361.
16 L. L. Zhang, S. Duan, X. L. Yang, G. Liang, Y. H. Huang, X. Z. Cao, J. Yang, S. B. Ni and M. Li, *Sci. Rep.*, 2014, **4**, 5064.

17 L. L. Zhang, S. Duan, X. L. Yang, G. Liang, Y. H. Huan, X. Z. Cao, J. Yang, M. Li, M. C. Croft and C. Lewis, *J. Power Sources*, 2015, **274**, 194–202.

18 C. Deng, S. Zhang, S. Y. Yang, B. L. Fu and L. Ma, *J. Power Sources*, 2011, **196**, 386–392.

19 J. P. Perdew, K. Burke and M. Ernzerhof, *Phys. Rev. Lett.*, 1996, **77**, 3865–3868.

20 G. Kresse and J. Furthmuller, *Phys. Rev. B: Condens. Matter Mater. Phys.*, 1996, **54**, 11169–11186.

21 G. Kresse and J. Hafner, *Phys. Rev. B: Condens. Matter Mater. Phys.*, 1993, **47**, 558–561.

22 H. J. Monkhorst and J. D. Pack, *Phys. Rev. B: Condens. Matter Mater. Phys.*, 1976, **13**, 5188–5192.

23 V. I. Anisimov, J. Zaanen and O. K. Andersen, *Phys. Rev. B: Condens. Matter Mater. Phys.*, 1991, **44**, 943–954.

24 C. Sirisopanaporn, C. Masquelier, P. G. Bruce, A. R. Armstrong and R. Dominko, *J. Am. Chem. Soc.*, 2011, **133**, 1263–1265.

25 M. M. Doeff, Y. Q. Hu, F. McLarnon and R. Kostecki, *Electrochem. Solid-State Lett.*, 2003, **6**, A207–A209.

26 J. Yang, L. Hu, J. Zheng, D. He, L. Tian, S. Mu and F. Pan, *J. Mater. Chem. A*, 2015, **3**, 9601–9608.

27 J. L. Yang, X. C. Kang, L. Hu, X. Gong and S. C. Mu, *J. Mater. Chem. A*, 2014, **2**, 6870–6878.

28 P. Mills and J. Sullivan, *J. Phys. D: Appl. Phys.*, 1983, **16**, 723.

29 P. A. Grutsch, M. V. Zeller and T. P. Fehlner, *Inorg. Chem.*, 1973, **12**, 1431–1433.

30 V. Subramanian, W. W. Burke, H. W. Zhu and B. Q. Wei, *J. Phys. Chem. C*, 2008, **112**, 4550–4556.

31 H. K. Wang, K. P. Dou, W. Y. Teoh, Y. W. Zhan, T. F. Hung, F. H. Zhang, J. Q. Xu, R. Q. Zhang and A. L. Rogach, *Adv. Funct. Mater.*, 2013, **23**, 4847–4853.

32 J. Ma, B. H. Li, H. D. Du, C. J. Xu and F. Y. Kang, *J. Solid State Electrochem.*, 2012, **16**, 1–8.

33 (*a*) A. R. Armstrong, N. Kuganathan, M. S. Islam and P. G. Bruce, *J. Am. Chem. Soc.*, 2011, **133**, 13031–13035; (*b*) D. H. Seo, H. Kim, I. Park, J. Hong and K. Kang, *Phys. Rev. B: Condens. Matter Mater. Phys.*, 2011, **84**, 220106.

34 C. Eames, A. R. Armstrong, P. G. Bruce and M. S. Islam, *Chem. Mater.*, 2012, **24**, 2155–2161.

35 Y. S. Li, X. Cheng and Y. Zhang, *J. Electrochem. Soc.*, 2012, **159**, A69–A74.

36 H. Y. Gao, Z. Hu, K. Zhang, F. Y. Cheng and J. Chen, *Chem. Commun.*, 2013, **49**, 3040–3042.